Ionics (2020) 26:1895–1911
https://doi.org/10.1007/s11581-019-03393-8

ORIGINAL PAPER

Effect of Zr^{4+} on the phase stability and oxygen permeation characteristics of $SrCo_{0.8}Fe_{0.2-y}Zr_yO_{3-\delta}$ ($y \leq 0.1$) membranes

Vijay Kumar Kashyap [1,2] · Shivendra Kumar Jaiswal [1,3] · Jitendra Kumar [1,4]

Received: 23 April 2019 / Accepted: 3 December 2019 / Published online: 8 January 2020

Abstract

A stable and high oxygen permeable membrane system has been developed via partial replacement of iron with zirconium in $SrCo_{0.8}Fe_{0.2}O_{3-\delta}$ compound. The initial powder series of composition $SrCo_{0.8}Fe_{0.2-y}Zr_yO_{3-\delta}$ ($0 \leq y \leq 0.1$), synthesized by an oxalate-based sol-gel route, is shown to exhibit a single perovskite-type cubic phase at 27 °C, transform to a brownmillerite (Ca_2AlFeO_5)-type orthorhombic structure, and finally assume a stable open cubic phase with disordered oxygen vacancies at temperatures determined by zirconium content, transitions being at 200 and 800 °C, respectively for the system $y = 0.05$. The highest J_{O2} of 2.54×10^{-6} mol cm^{-2} s^{-1} is realized in optimum composition of $y = 0.05$ at 1000 °C. The formation of cubic phase in Sr–Co–Fe–O system with abundance of disordered anion vacancies is crucial for both the high oxygen permeability and extended operational stability at elevated temperatures.

Keywords Sol-gel · Structural stability at elevated temperatures · Oxygen deficiency · XPS · Oxygen permeability

Introduction

The development of membranes with high oxygen permeability and adequate stability is desirable in highly efficient oxygen separation systems [1]. The perovskite-type oxides with general formula ABO_3 (A—rare earth or alkaline rare earth metal ions {Ba, Ca, Sr, La, etc.}; B—transition and other metal ions {Co, Fe, Zn, Mn, Ga, etc.}; O—oxygen ions) have been explored over the years for their oxygen permeation capacity and stability [2–5]. Their salient features include (i) a wide range of oxygen deficiency/vacancy, (ii) variable oxidation states of ions at A and/or B site, and (iii) mixed ionic and electronic conductivity. Consequently, $ABO_{3-\delta}$ (A = Sr, La; B = Co, Fe; δ = oxygen deficiency) perovskites have been studied widely for a variety of applications, viz., gas/oxygen separation as membrane, oxygen pumps, solid oxide fuel cells, oxidative coupling of methane as catalyst, oxygen sensors, etc. [6–9]. Teraoka et al. [10, 11] synthesized $Ln_{1-x}A_xCo_{1-y}B_yO_{3-\delta}$ (Ln = La, Pr, Nd, Sm, Gd; A = Sr, Ca, Ba; B = Mn, Cr, Fe, Co, Ni, Cu) ($x = 0$–0.4, $y = 0$–0.2) by solid-state reaction of metal acetates and nitrates at elevated temperatures (970–1300 °C) and measured their oxygen permeability (J_{O2}). Among them, $SrCo_{0.8}Fe_{0.2}O_{3-\delta}$ membrane (thickness ~ 1 mm) showed the highest J_{O2} of 2.31×10^{-6} mol cm^{-2} s^{-1} at 850 °C, but displayed limited-phase stability and mechanical steadiness [12–16]. Its noticeable high J_{O2} sustained interest in this $ABO_{3-\delta}$ system with continual investigations [17–21]. Consequently, the partial replacement of B species by zirconium (Zr) in $SrCo_{0.8}Fe_{0.2}O_{3-\delta}$ is reported to stabilize the perovskite-type cubic structure and induce disordering in oxygen vacancies [22, 23]. Also, the enhanced oxygen permeability in $La_{0.2}Ba_{0.8}Co_{0.8}Fe_{0.2-x}Zr_xO_{3-\delta}$ ($x = 0.05$) at elevated temperatures is attributed to prevailing disorder in anion vacancies [24]. Zirconium in $BaCo_{0.7}Fe_{0.3-x}Zr_xO_{3-\delta}$ ($x = 0$–0.12) is found to increase J_{O2} up to $x = 0.06$ (value being 2.7 ml min^{-1} cm^{-2} at 925 °C for 1-mm-thick membrane) but decrease at higher content [25]. Further, ZrO_2 containing $SrCo_{0.4}Fe_{0.6}O_{3-\delta}$ membrane displays high oxygen permeability (J_{O2}) and remains stable as well at elevated temperatures and reduced oxygen partial pressures [26]. In contrast, Yang

✉ Jitendra Kumar
jk@iitk.ac.in; jkiitk@gmail.com

[1] Materials Science Program, Indian Institute of Technology Kanpur, Kanpur 208016, India

[2] Present address: Department of Materials Science and Metallurgical Engineering, University Institute of Engineering and Technology, CSJM University, Kanpur 208025, India

[3] Present address: Department of Physics, National Institute of Technology, Patna, India

[4] Present address: 654 Race Course Valley, Dehradun, India

et al. [22, 23] found improved phase stability in $SrCo_{0.4}Fe_{0.6-x}Zr_xO_{3-\delta}$ ($x = 0$–0.2) membranes, but with noticeable decrease in oxygen permeability. Chen et al. [27] and Lu et al. [28] also observed analogous results (i.e., improved structural stability and reduced oxygen permeability) in Zr-doped $SrCo_{0.8}Fe_{0.2}O_{3-\delta}$ and $Ba_{0.5}Sr_{0.5}Co_{0.8}Fe_{0.2}O_{3-\delta}$ membranes, produced with powders prepared by EDTA and solid-state reaction method, respectively. Obviously, zirconium incorporation in $SrCo_{0.8}Fe_{0.2}O_{3-\delta}$ compound has led to conflicting oxygen permeability data which need to be resolved by further study. Thus, $SrCo_{0.8}Fe_{0.2-y}Zr_yO_{3-\delta}$ ($y = 0$–0.1) system becomes the natural choice and preferred for the present investigation. The objective has been to understand the effect of zirconium on its phase stability and oxygen permeability characteristics. The stability of perovskite structures is supposed to improve with addition of fixed valence state elements [27]. Also, increase in unit cell size (i.e., realizing a somewhat open structure) may facilitate movement of anions and enhance oxygen permeability. With fixed valency (4 +) and ionic radii larger than cobalt/iron species, besides being robust, zirconium is selected for incorporation in $SrCo_{0.8}Fe_{0.2}O_{3-\delta}$ to yield desirable material for oxygen permeable membrane application.

Solid-state reaction, citrate-EDTA complexing method, and acetic acid-based sol-gel route have been used over the years for synthesis of oxide powders for membrane purposes [29–32]. Among them, sol-gel is optimal and offers certain advantages, viz., homogeneous mixing of precursors at atomic level, better stoichiometry control, high purity, and low cost [32]. Hence, an oxalate-based sol-gel route is chosen here to prepare $SrCo_{0.8}Fe_{0.2-y}Zr_yO_{3-\delta}$ ($y \leq 0.10$) powders for (i) in situ phase evaluation by X-ray diffraction (XRD), (ii) determining oxidation states of species with relative amounts by X-ray photoelectron spectroscopy (XPS), and (iii) membrane making to get better insight about the material (with zirconium) in terms of oxygen permeability, phase stability, and continuous real operation at 900 °C.

Experimental

$SrCo_{0.8}Fe_{0.2-y}Zr_yO_{3-\delta}$ ($y = 0.$ 0.025, 0.050, 0.075, 0.10) powders were prepared by sol-gel technique using appropriate mol % of anhydrous strontium nitrate ($Sr(NO_3)_2$) (Qualigens), cobalt nitrate hexahydrate ($Co(NO_3)_2{\cdot}6H_2O$) (Loba), ferric nitrate nano-hydrate ($Fe(NO_3)_3{\cdot}9H_2O$) (Qualigens), zirconyl nitrate hydrate ($ZrO(NO_3)_2{\cdot}H_2O$) (Loba), and oxalic acid dihydrate ($C_2H_2O_4{\cdot}2H_2O$) (Rankem) as precursors. Ethyl alcohol/ethanol (C_2H_5OH) (Hayman) and distilled water were used as solvent. First, each precursor was separately dissolved in ~200 ml of ethanol at 35–40 °C under vigorous stirring for 30 min to get a transparent solution. Due to poor solubility of strontium nitrate and zirconyl nitrate in ethanol, approximately 5 ml of distilled water was added dropwise to achieve complete dissolution. Second, the nitrate salt solutions were poured in a tray and mixed thoroughly before adding oxalic acid solution gradually and the mixture was stirred continuously to form a dark orange gel. Third, the product was digested (i.e., left as such for reaction to occur) for 12 h, dried at 80 °C for 24 h, then ground using an agate mortar-pestle, and finally sieved to obtain a fine light almond color powder (presumably of oxalate; evident from a strong peak visible at 1640 cm^{-1} in its Fourier transform infra-red (FT-IR) spectrum) [33]. The dried sol-gel oxalate was finally decomposed at 950, 1150, and 1300 °C each for 5 h by raising the temperature at a rate of 3 °C/min. The product was then furnace cooled to room temperature. The resulting black $SrCo_{0.8}Fe_{0.2-y}Zr_yO_{3-\delta}$ ($y = 0$–0.10) powders were subjected to grinding and sieving (through a 240 mesh) for studying their morphology, structural stability, etc. For oxygen permeation measurements, pellets were made by pressing the powder in a die (size ~ 10-mm diameter) at a hydraulic pressure of 50 kN, then annealed at 1300 °C (by raising the temperature at a rate of 3 °C/min) for 5 h and cooled in furnace itself to room temperature. The pellets/discs/membranes (diameter ~ 10 mm and thickness 1–2 mm) so obtained correspond to relative density of better than 95% of the bulk value.

An X-ray diffractometer (PANalytical X'Pert PRO) with $CuK\alpha_1$ radiation (wavelength $\lambda = 1.540598$ Å) was engaged for identification of phases present and evaluation of their stability in the temperature range 27–1000 °C. A field emission scanning electron microscope (Carl Zeiss NTS GmbH- SUPRA 40VP) was used for observing the morphology of dried sol-gel products (presumably oxalates), oxide powders, and membranes. An X-ray photoelectron spectrometer (PHI 5000 Versa Probe, ULVAC-PHI) using $AlK\alpha$ (1486.6 eV) radiation was employed for ascertaining the oxidation states of iron and cobalt species. A laboratory reactor, combined with a gas chromatograph (NUCON, Model 5765) and a molecular sieve 5A capillary column, was employed for measuring the oxygen permeability of membranes in the temperature range of 700–1000 °C using air as feeding gas (400 ml/min) and helium as a carrier (45 ml/min). A fine alumina (size ~ 50 nm) paste–coated inconel washer served as sealant for $SrCo_{0.8}Fe_{0.2-y}Zr_yO_{3-\delta}$ ($y = 0$–0.10) membranes. The alumina paste was also applied over the side curved surface of the disc membrane to prevent radial leakage of oxygen in the reactor. The nitrogen content of the collected gas was simultaneously measured to allow correction in data for air leakage through pore and/or around the membrane. The membrane was maintained at each temperature for about

30–45 min to attain equilibrium before noting down the permeation reading.

Results and discussion

Microstructure and phases

The powder samples displayed different morphologies depending on the composition (Fig. 1). For example, numerous sticks lying parallel to each other in different groups (orienting randomly) are visible with some overlap at places–giving appearance of a thatched roof, mat, or nest of twigs in composition $y = 0$ (Fig. 1a). On the other hand, samples looked like algae or leaf for $y =$ 0.025 and 0.05 (Fig. 1b, c), islands/regions with gaps for $y =$ 0.075 (Fig. 1d), and bars/parallelepiped for $y = 0.10$ (Fig. 1e).

Figure 2 shows the weight (W%) and dW(%)/dT versus temperature plots of dried sol-gel powder, conforming to composition $SrCo_{0.8}Fe_{0.2-y}Zr_yO_{3-\delta}$ ($y = 0$, 0.05, and 0.10), obtained by raising the temperature at a rate of 4 °C per minute up to 900 °C in air. Three main stages of weight loss found correspond to removal of (i) water, (ii) crystallizing water and carbon monoxide, and (iii) residual CO and CO_2. The decomposition was nearly complete at ~ 900 °C with a total loss of about 54–57% for the compositions $y = 0$, 0.05, and 0.10. The presence of zirconium causes less reduction in weight above 300 °C but leads to abrupt significant loss in the temperature range of 600–665 °C. It means that volatile species are retained by strong bonds and released eventually above 600 °C. This difference perhaps facilitates the formation of algae/leaf or other morphology observed in oxalate powder containing zirconium.

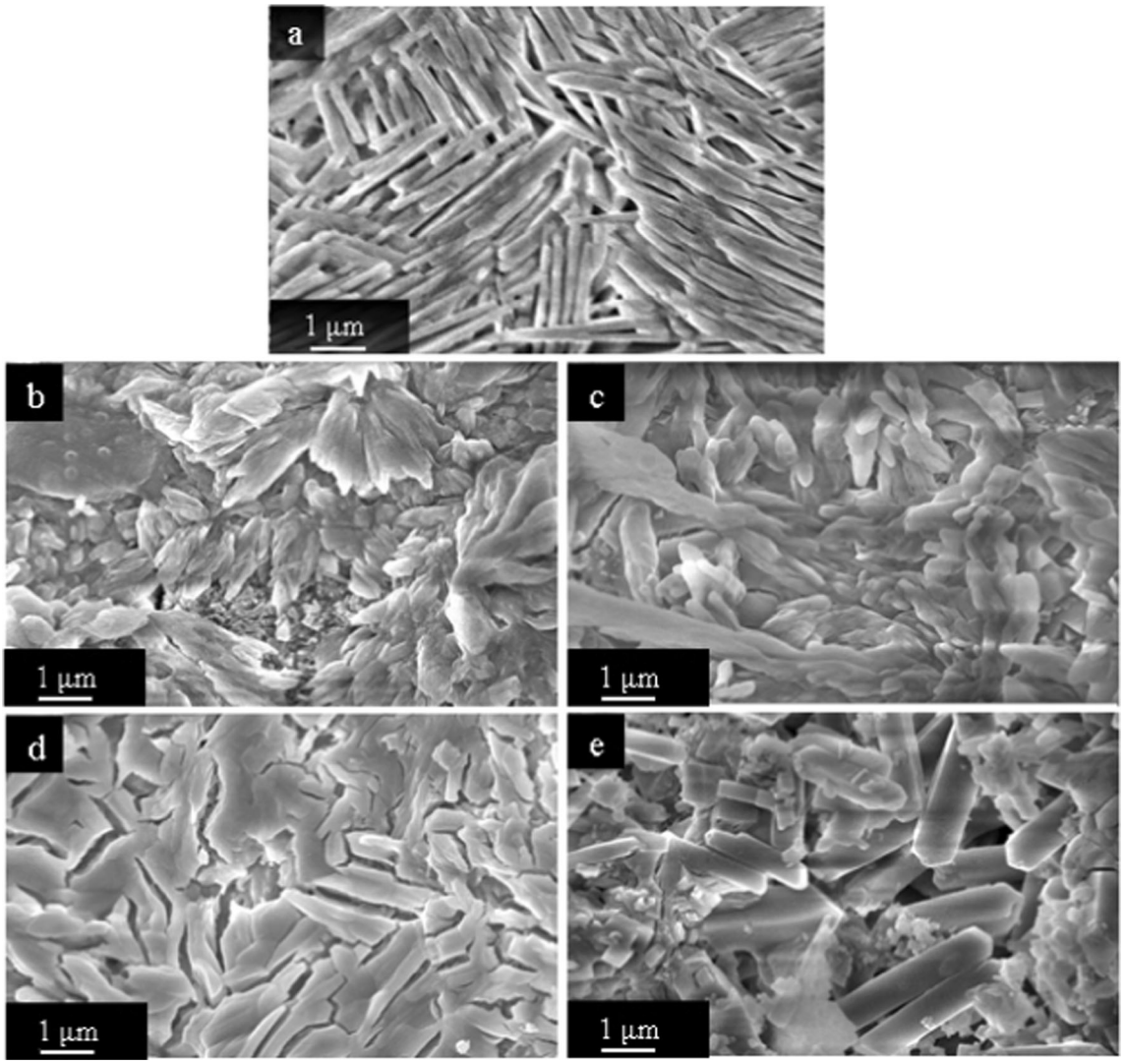

Fig. 1 Scanning electron micrographs (SE mode) of sol-gel products after drying at 80 °C for 24 h to yield $SrCo_{0.8}Fe_{0.2-y}Zr_yO_{3-\delta}$ with y equal to **a** 0, **b** 0.025, **c** 0.050, **d** 0.075, and **e** 0.100 following decomposition at elevated temperatures

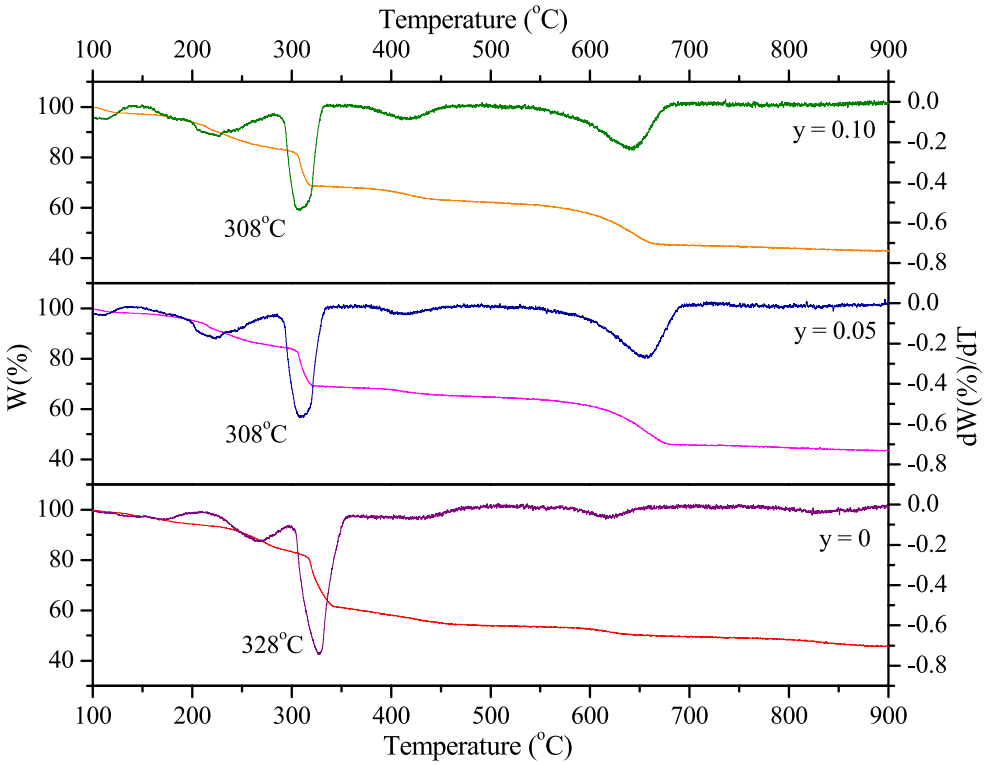

Fig. 2 Weight percent (W%) and d(W%)/dT versus temperature (T) plots of dried sol-gel product, synthesized for the preparation of $SrCo_{0.8}Fe_{0.2-y}Zr_yO_{3-\delta}$ with $y = 0$, 0.05, and 0.10

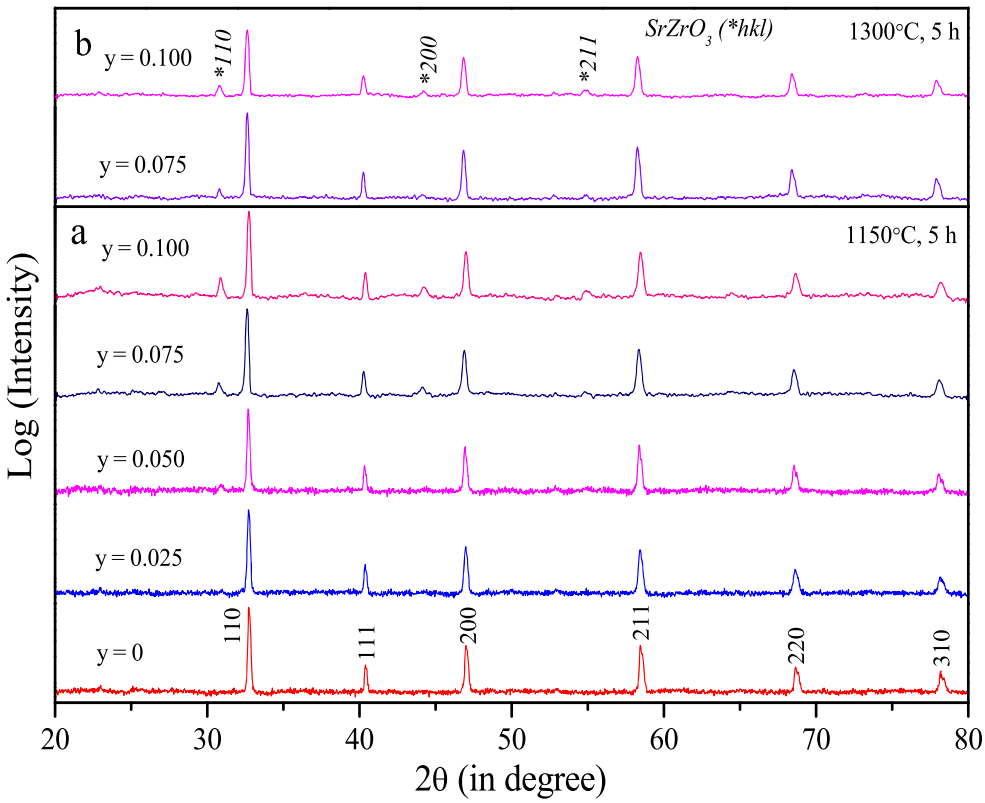

Fig. 3 X-ray diffraction patterns of $SrCo_{0.8}Fe_{0.2-y}Zr_yO_{3-\delta}$ obtained from dried sol-gel oxalate product after decomposition for 5 h each at (a) 1150 °C for $y = 0$, 0.025, 0.050, 0.075, and 0.010 and (b) 1300 °C for $y = 0.075$, and 0.100. The 110, 200, and 211 peaks of cubic $SrZrO_3$ ($a = 4.094$ Å) are marked by asterisk (*)

Figure 3 shows the XRD patterns of $SrCo_{0.8}Fe_{0.2-y}Zr_yO_{3-\delta}$ powders, obtained by decomposition of dried sol-gel oxalate product at 1150°or 1300 °C for 5 h in air. The diffraction patterns (Fig. 3a, b) of compositions $y = 0$ and 0.025 correspond to a single phase and can be indexed based on perovskite-type cubic structure with lattice parameter $a =$ 3.8650 and 3.8667 ± 0.0002 Å, respectively. Figure 3a matches well with $SrCo_{0.8}Fe_{0.2}O_{3-\delta}$ (JCPDS File no. 82-2445). At higher zirconium content ($y = 0.050$, 0.075, and 0.100), XRD contain some extra peaks (marked by asterisk (*) in Fig. 3) belonging to a secondary $SrZrO_3$ phase (JCPDS file no. 76-0167), which remain present even after sintering at 1300 °C for 5 h (Fig. 3b). This finding suggests that the solubility limit of zirconium in $SrCo_{0.8}Fe_{0.2}Zr_yO_{3-\delta}$ conforms to $y \leq 0.05$. The formation of $SrZrO_3$ has been observed earlier in $SrCo_{0.4}Fe_{0.6-x}Zr_xO_{3-\delta}$ ($x =$ 0.15, 0.2), $Sr(Co_{0.8}Fe_{0.2})_{1-x}Zr_xO_{3-\delta}$ ($x = 0.06$), $Sr(Co_{0.9}Zr_{0.1})O_{3-\delta}$, and $SrCo_{0.4}Fe_{0.5}Zr_{0.1}O_{3-\delta}$ systems as well [22, 27, 34, 35]. The analysis of XRD patterns reveal progressive increase in lattice parameter of perovskite-type $SrCo_{0.8}Fe_{0.2-y}Zr_yO_{3-\delta}$ cubic phase with rise in zirconium content (Fig. 3b); the values being 3.8650, 3.8667, 3.8690, 3.8758, and 3.8805 Å (± 0.0002 Å) for samples of compositions $y = 0$, 0.025, 0.050, 0.075, and 0.100, respectively. The increase in parameter (by ~ 0.4% maximum) may be attributed to partial substitution of iron ions with large zirconium species ($r_{Fe4+} = 0.585$ Å, $r_{Fe3+} = 0.55$ Å (low spin) or 0.645 Å (high spin), $r_{Zr4+} = 0.72$ Å). Obviously, zirconium insertion causes gradual expansion, increases the volume of $SrCo_{0.8}Fe_{0.2-y}Zr_yO_{3-\delta}$ cubic unit cell, and thus makes the structure somewhat open. The average crystallite size (D) of powder samples as deduced from the Scherrer formula ($D = 0.9\ x\ \lambda/(\beta \cos \theta)$, where λ is the wavelength of X-rays, β is the corrected full width at half maximum (FWHM), and θ is the Bragg angle), taking silicon as standard and diffraction data of 110 peak, turns out to be ~ 100 ± 2 nm for samples having no zirconium and in the range (79–118) ± 2 nm after zirconium addition. While the decrease in size is caused by impurity effect (addition of zirconium), the increase in D occurs due to grain growth brought by sintering at the elevated temperature (1300 °C), used for synthesis of compositions $y = 0.075$ and 0.100. D values of $SrCo_{0.8}Fe_{0.2-y}Zr_yO_{3-\delta}$ ($y = 0$, 0.025, 0.050, 0.075, and 0.010) powder samples are 100, 79, 83, 100, and 118 nm, respectively. Figure 4a displays a typical scanning electron micrograph of $SrCo_{0.8}Fe_{0.2}O_{3-\delta}$ powder sample obtained by decomposition of sol-gel derived oxalate at 1150° for 5 h. The corresponding zoom image shown in Fig. 4b indicates the presence of agglomerates of small crystallites. Similar morphology with no apparent variation is observed in samples containing zirconium.

Temperature induced phases

Figure 5a shows a few selected XRD patterns of a $SrCo_{0.8}Fe_{0.2}O_{3-\delta}$ sample, recorded at different temperatures in the range of 27–1000 °C. As discussed above, the pattern at 27 °C corresponds to a perovskite-type cubic unit cell with lattice parameter $a = 3.8650 \pm 0.0002$ Å. With increase in temperature, XRD pattern changes and the system appears transforming gradually to an orthorhombic phase assuming lattice parameters $a_o \sim a\sqrt{2}$, $b_o \sim 4a$, and $c_o \sim a\sqrt{2}$ (where "a" corresponds to the size of the primary $SrCo_{0.8}Fe_{0.2}O_{3-\delta}$ cubic unit cell) [18, 36–39]. Incidentally, this phase matches with the known brownmillerite (Ca_2AlFeO_5)-type orthorhombic structure having lattice parameters $a_o = 5.5981(3)$ Å, $b_o =$ 15.7832(8) Å, $c_o = 5.4692(3)$ Å, $Z = 4$, and space group Ibmm (JCPDF no. 82-2446), which supposedly have ordering of anionic vacancies. It can be described by composition $A^{2+}B^{3+}O_{2.5}$ ($A = Ca^{2+}$, $B = Al^{3+}$, Fe^{3+}) with BO_6 octahedra and BO_4 tetrahedra in alternating layers along the b-axis [40]. The crystal structure of a similar compound Ba_2InGaO_5 has been studied in detail by Didier et al. [41] recently. Accordingly, it displays a brownmillerite orthorhombic structure with cell parameters $a =$ 6.11239(4) Å, $b = 15.56492$ (2) Å, and $c = 5.92212(3)$ Å, $Z = 4$, and space group Ibm2 at 1100 °C. Indium and gallium ions are ordered and occupy octahedral and tetrahedral sites, respectively, because of their size difference (radii being $r_{In} = 0.80$ Å, $r_{Ga} = 0.62$ Å). A transition occurs at 1300 °C to a stable perovskite cubic structure assuming $a = 4.1539(9)$ Å, whereas the mixture of the two phases is observed in the intermediate temperature range (1100–1300 °C). The cubic phase depicts disordering of B-cations (In, Ga) as well as anions in $Ba_2In_2O_5$ and ascribed to high ionic conductivity [42]. Also,

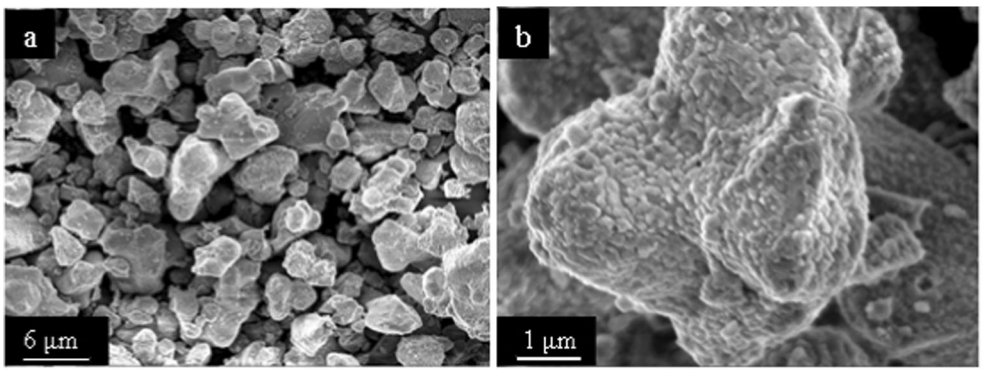

Fig. 4 Scanning electron micrographs (SE mode) of **a** $SrCo_{0.8}Fe_{0.2}O_{3-\delta}$ powder and its **b** zoom version of a lump showing agglomeration of small crystallites

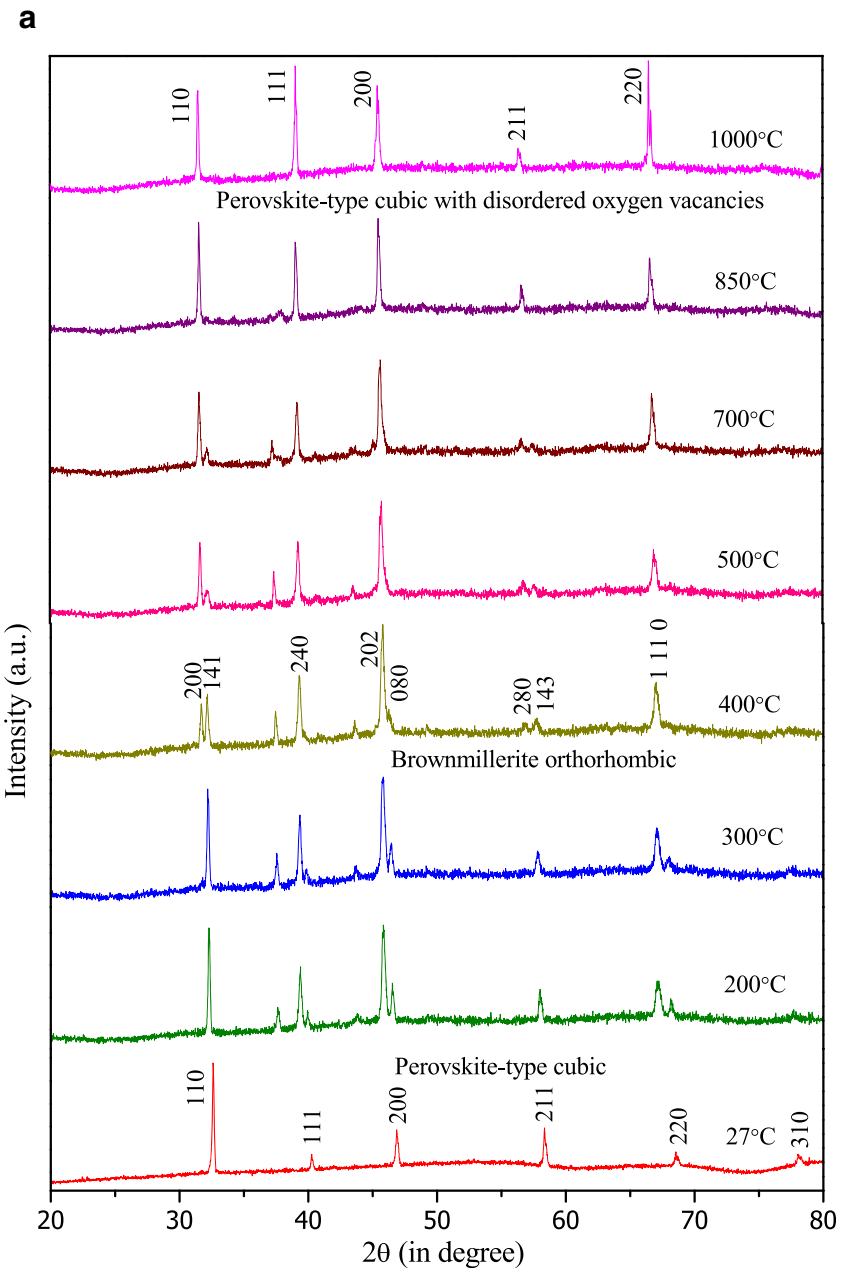

Fig. 5 **a** XRD patterns of a typical $SrCo_{0.8}Fe_{0.2}O_{3-\delta}$ (SCFO) powder sample at different temperatures in the range of 27°–1000 °C. **b** Summary of phases present in $SrCo_{0.8}Fe_{0.2-y}Zr_yO_{3-\delta}$ ($y = 0$, 0.025, 0.05, and 0.1) samples at different temperatures in the range of 27°–1000 °C

the above orthorhombic-cubic transition is reversible in nature. The split in the diffraction peak 110 of perovskite-type cubic is, in fact, indicative of the presence of a brownmillerite-type orthorhombic phase with oxygen vacancy ordering in $SrCo_{0.4}Fe_{0.6}O_{3-\delta}$ system [23]. Above 800 °C, a stable single perovskite-type cubic phase [17, 39] with increased lattice parameter ($a = 3.9937 \pm 0.0002$ Å) emerges at 1000 °C. The increase in "a" by ~ 3.3% can be ascribed to thermal expansion. Further, electrons released with oxygen desorption as molecules above 800 °C contribute in part for $B^{4+} \rightarrow B^{3+}$ conversion of Co and/or Fe species and, in turn, the B–O bond length stretches (i.e., increases) further. The weak B-O bonding relaxes the lattice strain and facilitates orthorhombic–cubic transformation besides disorder of oxygen vacancies perhaps. The weak B-O bonding relaxes the lattice strainand facilitates orthorhombic–cubic transformation besides disorder of oxygen vacancies perhaps. Since the orthorhombic structure has an ordered distribution of anion vacancies, movement of oxygen ions in that phase is somewhat restricted amounting to poor oxygen permeability [38]. The structural changes above 800 °C involve oxygen evolution with order → disorder transition of anion vacancies. Such a state is expected to facilitate oxygen flow in the new phase emerging above 800 °C with an enlarged perovskite-type cubic cell.

XRD diffraction patterns of $SrCo_{0.8}Fe_{0.2-y}Zr_yO_{3-\delta}$ ($y =$ 0.025–0.100) powders recorded in the temperature range of

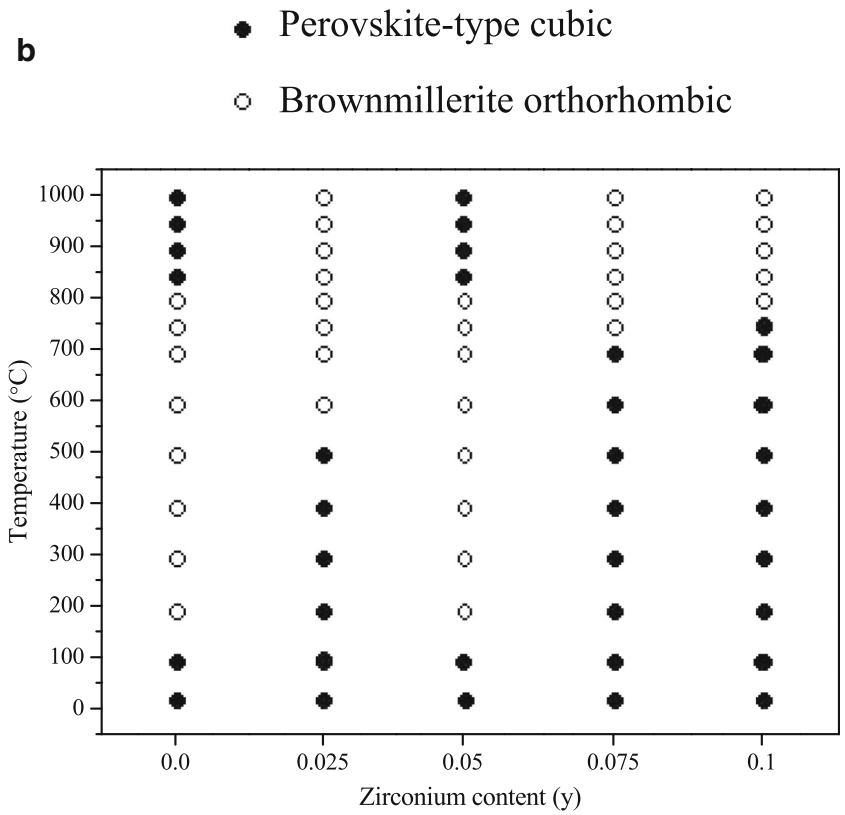

Fig. 5 continued.

27–1000 °C reveal interesting effects of zirconium, which can be summarized as under (Fig. 5b):

a) The temperature of cubic → brownmillerite orthorhombic-phase transition increases from 200 to 500 °C for the composition $y = 0.025$. However, for the case of $SrCo_{0.8}Fe_{0.2-y}Zr_yO_{3-\delta}$ ($y = 0.050$), the orthorhombic phase emerges at 200 °C itself (with little $SrZrO_3$) and remains stable up to 800 °C when it transforms back to cubic with enlarged unit cell, of course.
b) At zirconium content ($y = 0.075$ and 0.100), an added quantity of $SrZrO_3$ precipitates out and the cubic → orthorhombic transition occurs at 700 °C or above with the system becoming strontium deficient.
c) The orthorhombic phase exists in $SrCo_{0.8}Fe_{0.2-y}Zr_yO_{3-\delta}$ system above 500, 700, and 750 °C for compositions $y =$ 0.025, 0.075, and 0.100, respectively.
d) An enlarged stable perovskite cubic phase appears above 800 °C for the zirconium content $y = 0$ and 0.05.

The partial substitution of iron by zirconium in $SrCo_{0.8}Fe_{0.2}O_{3-\delta}$ modifies the average oxidation state of Fe/Co and, in turn, reduces the oxygen loss (δ). At $y = 0.050$, zirconium dissolution in $SrCo_{0.8}Fe_{0.2}O_{3-\delta}$ induces enough structural distortion due to its large size and facilitates cubic → orthorhombic transformation just above 100 °C. However, upon increasing zirconium content beyond $y = 0.050$, $SrZrO_3$ precipitates out with depletion of strontium and release of stress, if any. Consequently, initial perovskite cubic phase remains stable and transforms to orthorhombic phase only above 700–750 °C.

X-ray photoelectron spectroscopy studies

Figure 6 shows the XPS spectrum of $SrCo_{0.8}Fe_{0.2-y}Zr_yO_{3-\delta}$ ($y = 0$, 0.025, 0.050), obtained with a PHI 5000 Versa Probe photoelectron spectrometer model ULVAC using AlKα radiation (1486.6 eV) under vacuum of better than 6.7×10^{-8} Pa at a low resolution (step 1 eV) in the energy range of 0–900 eV. The peaks are identified as belonging to Sr3d, C 1 s + $Sr3p_{1/2}$, Co2p, Fe2p, O1s, and Zr3d levels. The carbon 1 s peak at 284.6 eV is treated as standard for calibration. The corresponding fine spectra were observed in different energy regimes at a high resolution (step 125 meV). The deconvoluted Gaussian peaks fitted using Origin 8.5 software for cobalt, iron, and oxygen are shown in Fig. 7. The values of binding energy for different species in $SrCo_{0.8}Fe_{0.2-y}Zr_yO_{3-\delta}$ ($y = 0$, 0.025, 0.050) system are summarized in Table 1. Their nature can now be discussed separately:

(a) Co 2p

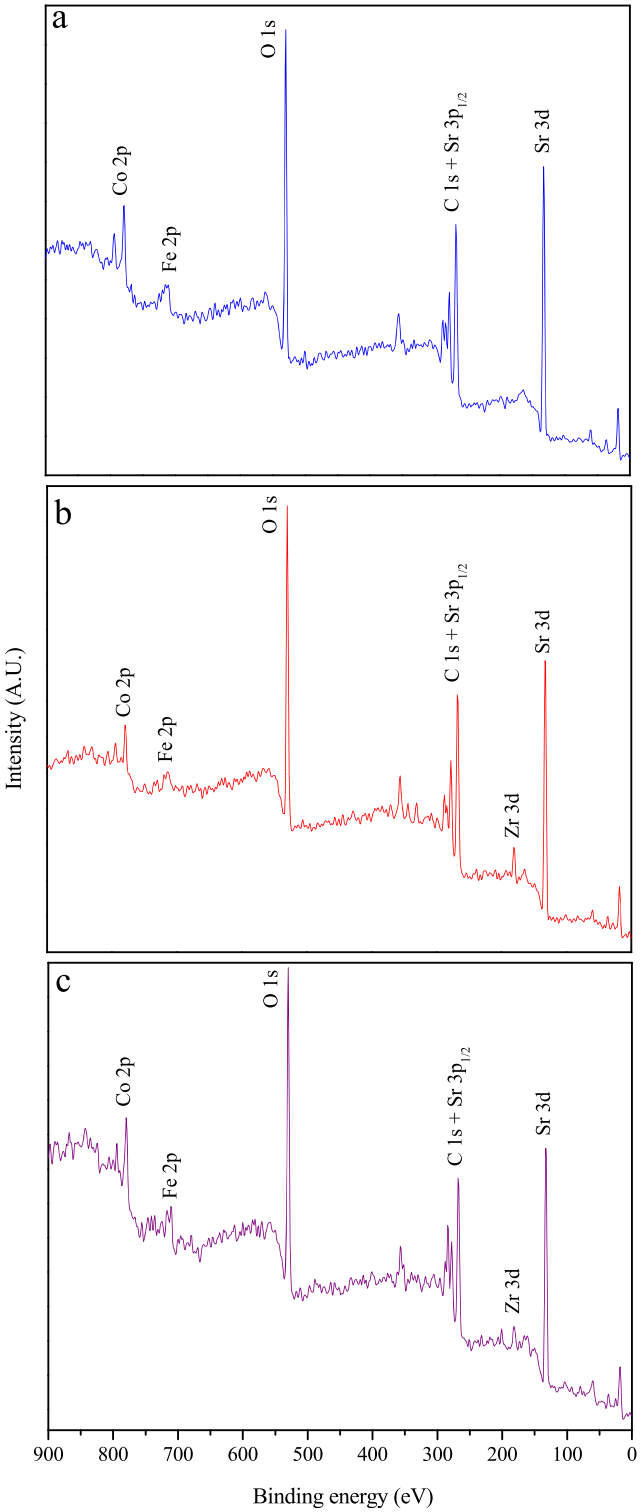

Fig. 6 XPS survey spectra of $SrCo_{0.8}Fe_{0.2-y}Zr_yO_{3-\delta}$ with $y = (a)\ 0$, (b) 0.025, and (c) 0.050

Figure 7(a1) depicts a high-resolution XPS scan of $SrCo_{0.8}Fe_{0.2}O_{3-\delta}$ in the energy range of 771–816 eV with two peaks of Co $2p_{3/2}$ and Co $2p_{1/2}$ levels. Dupin et al. [47] have described the XPS spectra of cobalt in $Li_{0.66}CoO_2$ and $LiCoO_2$ systems in detail. Accordingly, Co 2p peak appearing in the energy range 775–800 eV is built up of signals from cobalt (3 +) and (4 +) states. While a doublet with energies 779.8 and 795 eV corresponds to Co^{3+} ions, the other doublet with peaks at 781.5 and 796.8 eV belongs to Co^{4+} ions. In the present case, de-convolution exercise of XPS spectrum presented in Fig. 7(a1) reveals two doublets with binding energies (779.8 and 795.1 eV) and (781.4 and 796.7 eV). They can therefore be ascribed to Co^{3+} and Co^{4+} ions, respectively. The peak position and (%) peak area of each oxidation state as deduced from Co $2p_{3/2}$ peaks (Fig. 7(a1, a2,a3)) are listed in Table 2.The relative amounts of Co^{3+} and Co^{4+} ions, given by respective peak areas are 55.9% and 44.1%, respectively, in the case of $SrCo_{0.8}Fe_{0.2}O_{3-\delta}$ system.

(b) Fe 2p

Figure 7(b_1) shows a high-resolution XPS scan of $SrCo_{0.8}Fe_{0.2}O_{3-\delta}$ in the energy range 701–741 eV and contains information about the oxidation states of iron. The peak broadness at first sight suggests the presence of all three Fe^{3+}, Fe^{2+}, and Fe^{4+}ions, arising due to electrostatic interactions, spin-orbit coupling between the 2p core hole and unpaired 3d electrons of the photo-ionized cation, and crystal field effects [48, 49]. Yunfei et al. [46] have classified peaks of Fe $2p_{3/2}$ level in the energy range of 709.6–709.9 eV, 710.9–711.9 eV, and 712–714 eV for Fe^{2+}, Fe^{3+}, and Fe^{4+}species, respectively. The Gaussian fitting of Fe 2p shown in Fig. 7(b1) corresponds to two peaks with binding energy 710.9 and 714.2 eV, which can be attributed to Fe^{3+} and Fe^{4+} ions, respectively (Table 2). The peak position, % peak area, and oxidation state obtained from Fe $2p_{3/2}$ peaks (Fig. 7(b1, b2, b3)) are summarized in Table 2. Note that the Fe^{3+} ions present in $SrCo_{0.8}Fe_{0.2}O_{3-\delta}$ system is just 8.5% while the Fe^{4+} species share the remaining 91.5%.

(c) O 1 s

The high-resolution XPS spectrum in the energy range 525–543 eV depicted in Fig. 7(c1) gives the signature of oxygen ions. The Gaussian fitting of peak shows splitting and associated binding energies are 529.5 and 531.3 eV (Fig. 7(c1)). Machocki et al. [50] identified two peaks for oxygen in the XPS spectrum of manganese-lanthanum oxides: (i) at lower binding energy (529.4–529.8 eV) belonging to oxygen ion (O^{2-}) and (ii) slightly higher energy range of 531.2–531.8 eV arising due to O 1 s states of surface adsorbed oxygen (O_2^{2-}, O_2^-, or O^-). Thus, peaks of O 1 s observed at 529.5 and 531.3 eV can be assigned to oxygen ion (O^{2-}) and surface adsorbed oxygen, respectively. The peak position, % peak area, and nature of oxygen resulting from O 1 s peaks (Fig.

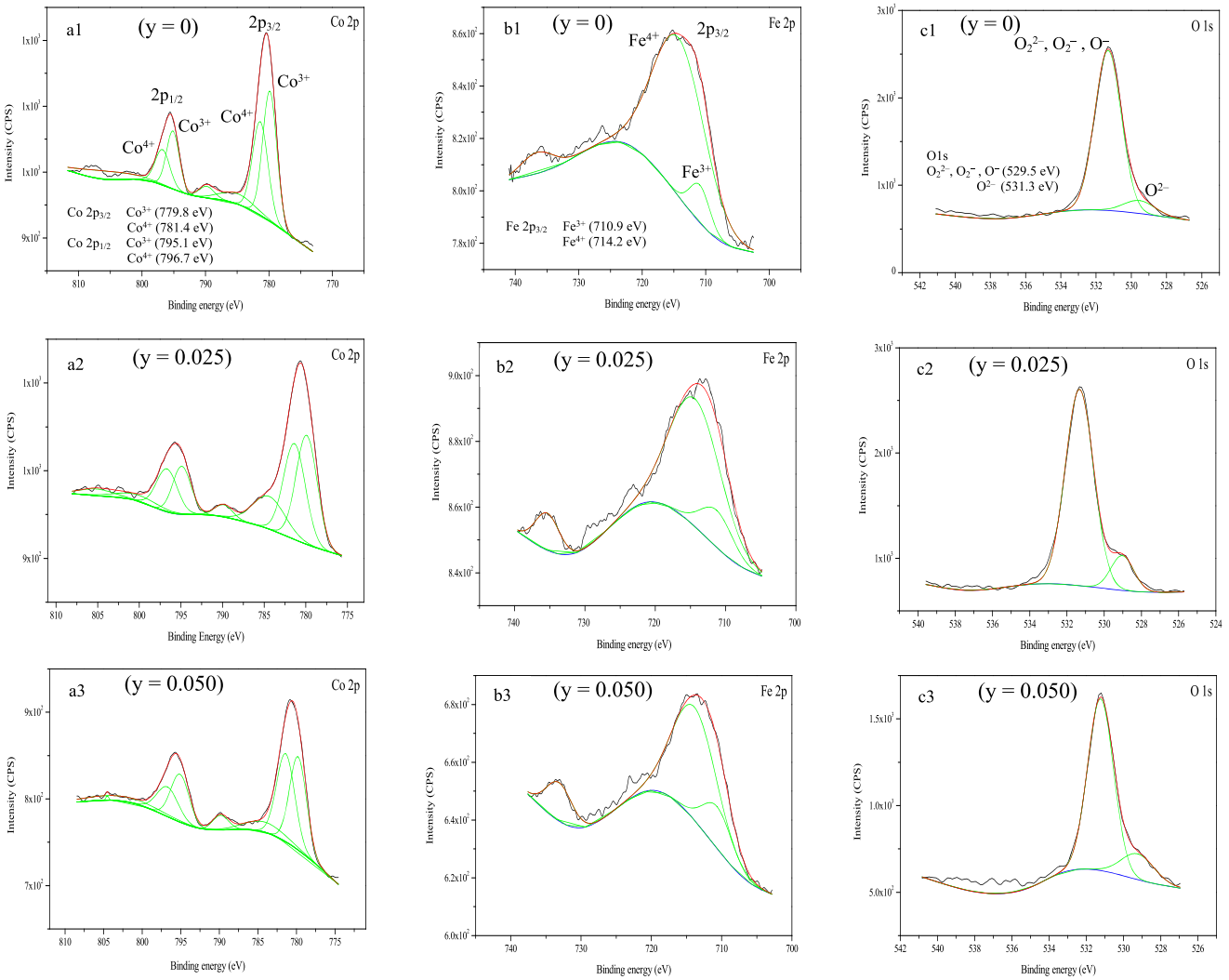

Fig. 7 XPS spectra showing Gaussian fitting of peaks for (a_1, a_2, a_3) Co 2p, (b_1, b_2, b_3) Fe 2p, and (c_1, c_2, c_3) O 1 s in $SrCo_{0.8}Fe_{0.2-y}Zr_yO_{3-\delta}$ ($y = 0$, 0.025, 0.050) system

7(c1, c2, c3)) in $SrCo_{0.8}Fe_{0.2}O_{3-\delta}$ are given in Table 2. These indicate that the surface adsorbed oxygen (O_2^{2-}, O_2^-, or O^-) amounts to 91.4% whereas the bulk oxygen ion (O^{2-}) is just 8.6%.

(d) Zr 3d

Zhang et al. [44] have resolved the Zr 3d spectrum and assigned binding energies 184.4 eV and 182.0 eV to Zr $3d_{3/2}$ and Zr $3d_{5/2}$, respectively, in close agreement with the stoichiometric ZrO_2 data. Accordingly, XPS peaks observed in Fig. 6b at 183.1 and 180.8 eV correspond to Zr $3dp_{3/2}$ and Zr $3d_{5/2}$ level, respectively, for $SrCo_{0.8}Fe_{0.2-y}Zr_yO_{3-\delta}$ ($y = 0.025$). These peaks shift to higher values 183.3 eV and 181.1 eV, respectively, when the zirconium content is increased to $y = 0.05$.

The relative amounts of cobalt and iron species in 3 + and 4 + oxidation states deduced from XPS data of $SrCo_{0.8}Fe_{0.2-y}Zr_yO_{3-\delta}$ ($y = 0$, 0.025, 0.050) are summarized in Table 3. These clearly point out that zirconium addition induces steady (i) decrease in Co^{3+} and Fe^{4+} species and (ii) increase in Co^{4+} and Fe^{3+} ions in $SrCo_{0.8}Fe_{0.2-y}Zr_yO_{3-\delta}$ ($y = 0$, 0.025, 0.050). Thus, zirconium (which is in 4 + oxidation state) replaces Fe^{4+} species in $SrCo_{0.8}Fe_{0.2}O_{3-\delta}$ and reduces their number. In addition, there is (i) proportionate $Co^{3+} \rightarrow Co^{4+}$change accompanied by release of electrons and (ii) some $Fe^{4+} \rightarrow Fe^{3+}$conversion with consumption of electrons. The net result is an effective increase in species of 4 + oxidation state with rise in zirconium amount (Table 3). There should therefore be a corresponding increase in oxygen ions (or decrease in anion vacancies, i.e., reduction in δ) for ensuring charge neutrality(discussed in the "X-ray photoelectron spectroscopy studies" section). The oxygen gain by the material can account for the changes in the oxidation states of species. The additional oxygen molecules adsorb turned into anions by consuming electrons released via $Co^{3+} \rightarrow Co^{4+}$ conversion. The

Table 1 XPS peak positions for $SrCo_{0.8}Fe_{0.2-y}Zr_yO_{3-\delta}$ system with $y = 0$, 0.025, and 0.05

Compound	Level	Binding energy (eV)	Ref.	SCFZO Binding energy (eV) for		
				$y = 0$	$y = 0.025$	$y = 0.050$
Strontium	Sr $3d_{5/2}$	133.0 (Sr^{2+})	[43]	133.2	133.2	133.2
	Sr $3d_{3/2}$	135.0 (Sr^{2+})	[43]	134.8	134.8	134.8
	Sr $3p_{3/2}$	267.6 (Sr^{2+})	[43]			
	Sr $3p_{1/2}$	279.6 (Sr^{2+})	[43]	279.3		
Carbon	C 1 s	285.0	[43]	284.6	284.6	284.6
		289.5	[43]	289.2	289.2	289.2
Zirconium	Zr $3d_{5/2}$	182.0 (Zr^{4+})	[44]	–	180.8	181.1
	Zr $3d_{3/2}$	184.4 (Zr^{4+})	[44]	–	183.1	183.3
Oxygen	O 1 s	529.4–529.8 (O^{2-})	[45]	529.5	529.0	529.2
		531.2–531.8 (O_2^-, O_2^{2-}, O^-)	[45]	531.3	531.3	531.2
Iron	Fe $2p_{3/2}$	710.9–711.9 (Fe^{3+})	[46]	710.9	711.3	710.6
		712.0–714.0 (Fe^{4+})	[46]	714.2	714.4	713.9
Cobalt	Co $2p_{3/2}$	779.8 (Co^{3+})	[47]	779.7	779.9	779.8
		781.5 (Co^{4+})	[47]	781.4	781.4	781.4
	Co $2p_{1/2}$	795.0 (Co^{3+})	[47]	795.1	794.9	795.1
		796.8 (Co^{4+})	[47]	796.8	796.7	796.7

oxygen gain is evident from the XPS analysis given in Table 2 as O^{2-} content is increasing progressively with rise in zirconium content y (= 0.025 and 0.050) in $SrCo_{0.8}Fe_{0.2-y}Zr_yO_{3-\delta}$.

Oxygen deficiency parameter (δ)

The oxygen deficiency parameter (δ) in $SrCo_{0.8}Fe_{0.2-y}Zr_yO_{3-\delta}$ can be estimated with the principle of charge balance, taking the oxidation states of iron and cobalt as 3 + and/or 4 +, and by considering variation in their contents. The structural formula can therefore be rewritten as $Sr^{2+}Co^{3+}{}_{0.8-x}Co^{4+}{}_xFe^{3+}{}_{0.2-y-z}Fe^{4+}{}_zZr^{4+}{}_yO^{2-}{}_{3-\delta}$ with $\delta = (1-x-y-z)/2$, where $x = (0–0.8)$, $y = (0–0.1)$, and $z = (0–0.2)$ denote Co^{4+}, Zr^{4+}, and Fe^{4+} content, respectively. In the ideal case, δ is zero where A and B sites in perovskite cubic structure (ABO_3) assume oxidation state 2 + and 4 +, respectively. However, if B species display both 3 + and 4 + states, δ becomes non-zero, indicating presence of oxygen vacancies. The value of "δ" lies in the range 0–0.5. Notice that δ, besides Zr^{4+} content, depends on the relative amounts of (Fe^{3+}, Fe^{4+}) and (Co^{3+}, Co^{4+}). XPS analysis was used to estimate the relative amounts of oxidation states of iron and cobalt species lying on the surface of the membranes. According to Table 2, $SrCo_{0.8}Fe_{0.2}O_{3-\delta}$ contains cobalt and iron ions in oxidation state (4 +) and (3 +) with oxygen species (O_2^{2-}, O_2^-, or O^-). The contents of species as found are Co^{4+} (44.11%), Co^{3+} (55.89%), Fe^{4+} (91.5%), Fe^{3+} (8.5%), surface adsorbed oxygen O_2^{2-}, O_2^-, or O^- (91.4%), and bulk oxygen O^{2-} (8.6%). Zirconium incorporation at Co/Fe sites leads to increase of Co^{4+}, Fe^{3+}, and O^{2-} ions while decrease of Co^{3+}, and Fe^{4+}

Table 2 Relative amount of cobalt, iron, and oxygen species in $SrCo_{0.8}Fe_{0.2-y}Zr_yO_{3-\delta}$ (for $y = 0$, 0.025, and 0.050) obtained from XPS spectra

Composition (y)	Cobalt (Co $2p_{3/2}$)			Iron (Fe $2p_{3/2}$)			Oxygen(O1s)		
	XPS peak position (eV)	% area	Oxidation state	XPS peak position (eV)	% area	Oxidation state	XPS peak position (eV)	% area	Oxygen type
0	779.86	55.9	3+	710.92	8.5	3+	531.32	91.38	Adsorbed oxygen
	781.37	44.1	4+	714.25	91.5	4+	529.53	8.63	Oxygen O^{2-}
0.025	779.90	52.3	3+	711.26	15.6	3+	531.33	87.57	Adsorbed oxygen
	781.36	47.7	4+	714.35	84.4	4+	529.03	12.43	Oxygen O^{2-}
0.050	779.79	49.6	3+	710.62	19.7	3+	531.23	84.18	Adsorbed oxygen
	781.40	50.4	4+	713.87	80.3	4+	529.24	15.82	Oxygen O^{2-}

Table 3 Fraction amounts in $SrCo_{0.8}Fe_{0.2-y}Zr_yO_{3-\delta}$ (for $y = 0$, 0.025, and 0.050)

Composition (y)	3 + oxidation state			4 + oxidation state			
	Fe^{3+}	Co^{3+}	Total (3 +)	Fe^{4+}	Co^{4+}	Zr^{4+}	Total (4 +)
0	0.017	0.447	0.464	0.183	0.353	0	0.536
0.025	0.027	0.419	0.446	0.148	0.381	0.025	0.554
0.050	0.030	0.397	0.427	0.120	0.403	0.050	0.573

ions. The net effect amounts to increase of total positive charge as well as number of oxygen O^{2-} ions (i.e., lowering of δ). Considering the relative amounts of Co^{3+}, Co^{4+}, Fe^{3+}, and Fe^{4+} present, oxygen deficiency parameter (δ) has been deduced by invoking the concept of charge neutrality. This exercise gives the value of δ as 0.23, 0.22, and 0.21 for $SrCo_{0.8}Fe_{0.2-y}Zr_yO_{3-\delta}$ with $y = 0$, 0.025, and 0.050, respectively. Obviously, there is minor decrease in oxygen deficiency parameter δ (or increase in anion concentration) with the increase in zirconium content. The above figures no doubt pertain to sample surface at room temperature, yet very useful in understanding the phenomenon at high temperatures.

Oxygen permeability

The oxygen permeation flux (J_{O2}) is specified in units of milliliters per square centimeter per minute or moles per square centimeter per second; the conversion relation being 1 ml cm^{-2} $min^{-1} = 7.44 \times 10^{-7}$ mol cm^{-2} s^{-1}. J_{O2} was measured in $SrCo_{0.8}Fe_{0.2-y}$ $Zr_yO_{3-\delta}$ ($y = 0$–0.1) membrane discs (diameter ~ 10 mm and thickness ~ 1.0–2.0 mm) at 700–1000 °C with air as a feeder gas on the front (or input) and helium as a carrier on the exit (or sweep) side [51]. Figure 8a depicts (J_{O2}) versus temperature plots for $SrCo_{0.8}Fe_{0.2}O_{3-\delta}$ membranes (thickness 1.0, 1.5, and 2.0 mm; effective diameter 8.8 mm), obtained using input air and sweeping helium gas flow rates of 400 ml/min and 45 ml/min, respectively. It may be noticed that J_{O2} increases with temperature invariably and is more for a thin membrane, and attains a maximum value of ~ 2.44 ml/cm^2·min (or 1.8×10^{-6} mol cm^{-2} s^{-1}) at 1000 °C for 1.0 mm-thick disc. The corresponding ln (J_{O2}) vs. 1000/T plots are shown in Fig. 8b. They are nearly linear and follow the Arrhenius equation $J_{O2} = J_O \exp(-E_A/k_BT)$, where Jo is the pre-exponential factor, E_A is the activation energy of oxygen permeation, and k_B is the Boltzmann constant. The values of activation energy, as deduced from the slopes of linear portions in the temperature range 800–1000 °C, are 50.0, 52.4, and 56.2 kJ/mol (or 0.52, 0.54, and 0.58 eV/ion) for membranes of thickness 1.0, 1.5, and 2.0 mm, respectively. The increase in E_A is in conformity with the observed decrease in the oxygen permeation flux for thicker membranes.

Earlier, $SrCo_{0.8}Fe_{0.2}O_{3-\delta}$ membranes were fabricated with powders derived from liquid citrate and solid-state reaction routes. The maximum oxygen permeability flux (J_{O2}) of 1-mm-thick membrane was found to be 1.8×10^{-7} or 6.3×10^{-7} mol cm^{-2} s^{-1} at 850 °C [17, 18]. However, Teraoka

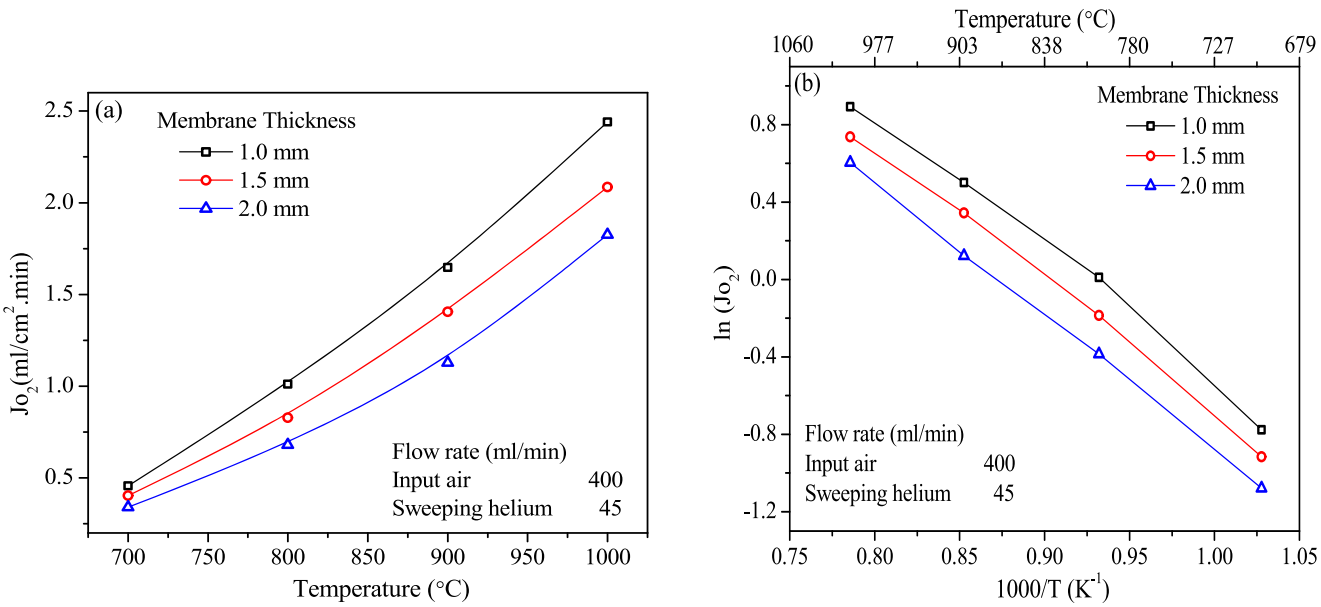

Fig. 8 **a** Oxygen permeation flux (J_{O2}) versus temperature and **b** ln (J_{O2}) vs. 1000/T Arrhenius plots of $SrCo_{0.80}Fe_{0.20}O_{3-\delta}$ membranes of thickness 1.0, 1.5, and 2.0 mm (diameter of each being ~ 10 mm)

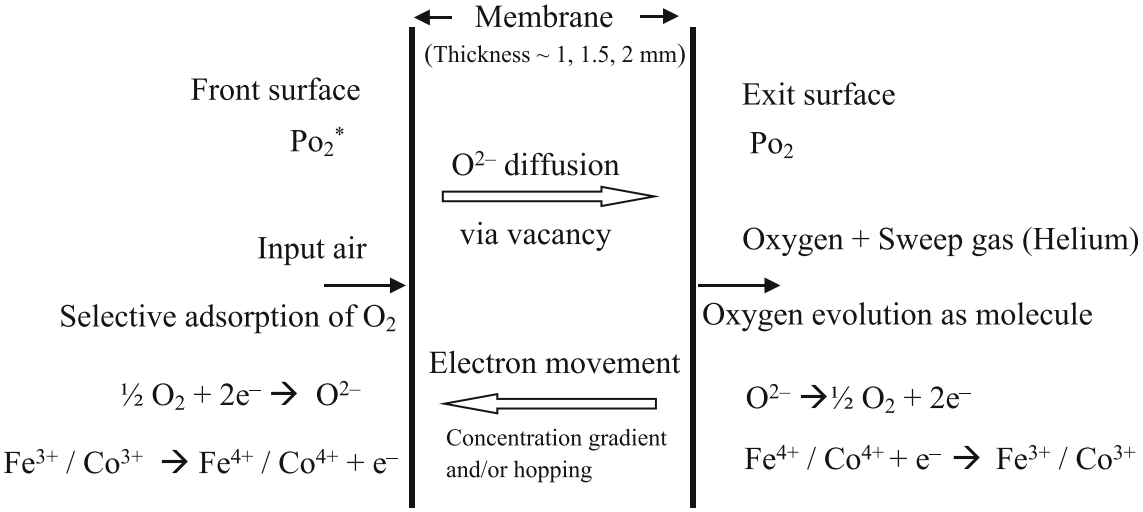

Fig. 9 Schematic diagram illustrating processes occurring at front and exit surface, oxygen transport, and electron movement in a typical $SrCo_{0.8}Fe_{0.2}O_{3-\delta}$ membrane

et al. [11] reported a value of 2.31×10^{-6} mol cm^{-2} s^{-1} (i.e., an order higher) in this system under similar operating conditions. The reason for this discrepancy is not apparent and remains still unanswered. It is another matter that significant variation in J_{O2} is usually observed even in identical membranes [29]. In the present study, J_{O2} value of $SrCo_{0.8}Fe_{0.2}O_{3-\delta}$ membrane (thickness 1.0 mm), fabricated using sol-gel-based powder, is slightly higher $\sim 9.9 \times 10^{-7}$ mol cm^{-2} s^{-1} (or 1.33 ml cm^{-2} min^{-1}) at 850 °C (with input air flow rate of 400 ml/min and sweeping helium flow rate of 45 ml/min) than those reported by Kruidhof et al. [17] and Qiu et al. [18], respectively. The improvement in J_{O2} has origin with high purity powder and a mechanically stable membrane [31, 52]. It is due to homogeneous powder of fine particles and, in turn, a stable compact disc of high density (> 95%) obtained via sol-gel route (preferred here over solid-state reaction), which ensures steady and full mixing of precursor species at the atomic/ molecular level and provides better stoichiometry control.

The processes occurring at front and exit surfaces and within the membrane disc are illustrated schematically in Fig. 9. A driving force for oxygen permeation is the partial pressure gradient prevailing along the membrane thickness. The main steps involved in permeation process are:

(a) selective adsorption of oxygen molecules on the front surface (at high pressure) and their dissociation into ions by capturing electrons following the reaction $O_2 + 4e^- \rightarrow 2O^{2-}$,
(b) migration/diffusion of oxygen ions through the membrane thickness via anion vacancies to the exit (sweeping) side,
(c) conversion of oxygen ions into molecules by leaving behind the electrons before desorbing at the exit surface, the reaction being $2O^{2-} \rightarrow O_2 + 4e^-$, and
(d) movement of electrons backwards from the exit to the front side of the membrane due to concentration gradient and/or via hopping following the scheme

$$B^{3+}–O^{2-}–B^{4+} \rightarrow B^{4+}–O^{2-}–B^{3+} (B = Co, Fe)$$

At elevated temperatures, J_{O2} increases due to cumulative effects of (i) additional anion vacancy generation, (ii) enhanced surface reactions/improved dissociation of oxygen molecules, and (iii) easy forward migration of O^{2-} ions and backward movement of electron within the membrane.

The partial replacement of B species by zirconium (Zr) in $SrCo_{0.8}Fe_{0.2}O_{3-\delta}$ stabilizes the perovskite-type cubic structure and induces disordering in oxygen vacancies as well [22, 23]. Also, increased oxygen permeability of $La_{0.2}Ba_{0.8}Co_{0.8}Fe_{0.2-x}Zr_xO_{3-\delta}$ ($x = 0.05$) at elevated temperatures is attributed to prevailing disorder in anion vacancies [24]. Zirconium in $BaCo_{0.7}Fe_{0.3-x}Zr_xO_{3-\delta}$ ($x = 0$–0.12) increases J_{O2} up to $x =$ 0.06 but decreases at higher content [25]. Further, ZrO_2 containing $SrCo_{0.4}Fe_{0.6}O_{3-\delta}$ membrane not only depicts better oxygen permeability (J_{O2}) but also remains stable at elevated temperatures and under reduced oxygen partial pressures [26]. On the contrary, Yang et al. [22, 23] observed improved phase stability in $SrCo_{0.4}Fe_{0.6-x}Zr_xO_{3-\delta}$ ($x = 0$–0.2) membranes at the cost of perceptible decrease in oxygen permeability. Chen et al. [27] and Lu et al. [28] also reported similar results (i.e., improved structural stability and reduced oxygen permeability) in Zr-doped $SrCo_{0.8}Fe_{0.2}O_{3-\delta}$ and $Ba_{0.5}Sr_{0.5}Co_{0.8}Fe_{0.2}O_{3-\delta}$ membranes, respectively. Obviously, zirconium incorporation in $SrCo_{0.8}Fe_{0.2}O_{3-\delta}$ compound has led to conflicting oxygen permeability data. The stability of perovskite structure is also known to improve with addition of fixed valence state elements [27]. Further, increase in unit cell size (i.e., realizing a somewhat open structure) may

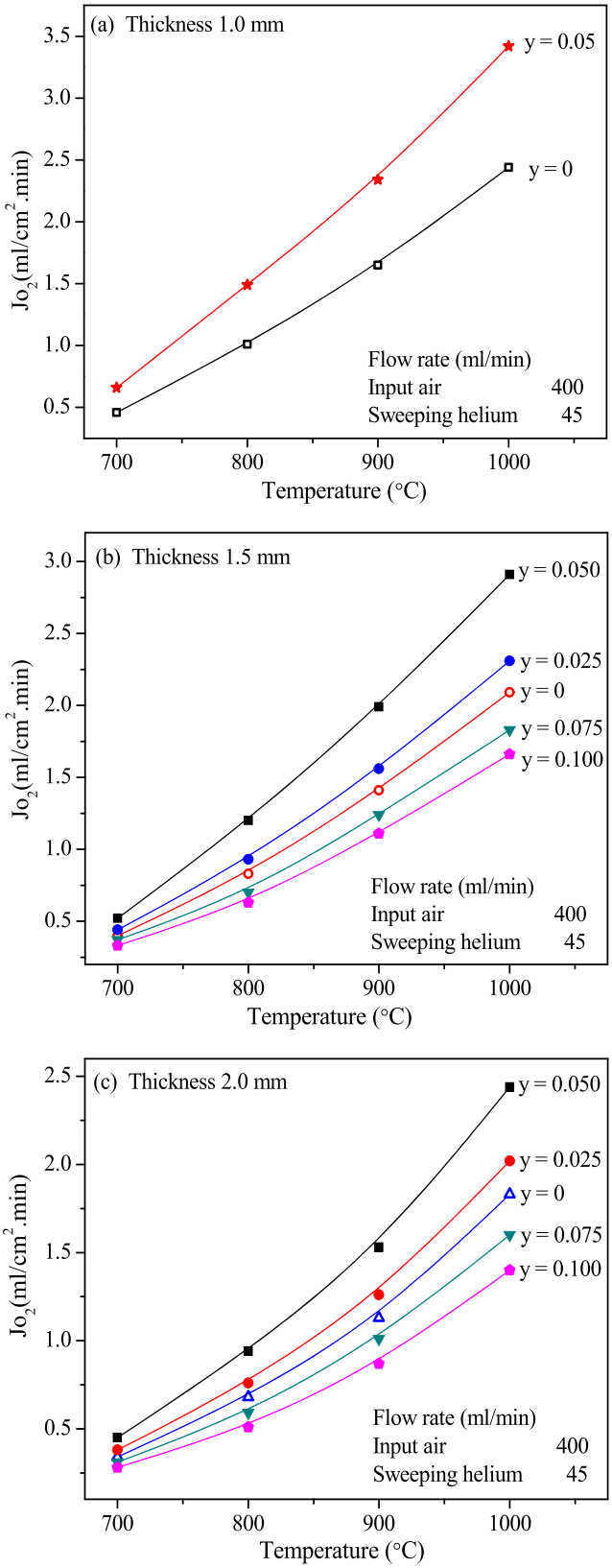

Fig. 10 Oxygen permeation flux (J_{O2}) versus temperature plots of $SrCo_{0.80}Fe_{0.20-y}Zr_yO_{3-\delta}$ membranes of diameter ~ 10 mm and thickness **a** 1.0 mm, **b** 1.5 mm, and **c** 2.0 mm

facilitate movement of anions and enhance oxygen permeability. With zirconium, oxygen vacancy concentration should decrease due to its oxidation state (4 +) and is reflected in room temperature XPS data as well. However, membrane operates at elevated temperatures where some oxygen evolution also occurs and compensates for the loss.

The effect of zirconium on oxygen permeation of $SrCo_{0.8}Fe_{0.2-y}Zr_yO_{3-\delta}$ ($y = 0$–0.10) membranes (thickness 1, 1.5, and 2 mm) at 700–1000 °C is shown in Fig. 10. The measurements were repeated 3–4 times in each case for consistency and data reliability. Accordingly, zirconium insertion enhances the oxygen permeability initially (up to $y = 0.05$) but reduces at higher concentrations at all temperatures (Table 4). As for example, 1.5-mm-thick membrane at 1000 °C reveals increase in J_{O2} to 2.91 ml/cm^2·min for the Zr content $y = 0.05$ but exhibits a lower value of 1.66 ml/cm^2·min for $y = 0.10$. Notice that J_{O2} value for 1-mm-thick membrane at 1000 °C advances from 2.44 ml/cm^2·min to 3.42 ml/cm^2·min when zirconium content (y) increases from 0 to 0.05. Thus, 5% zirconium at B site (initially occupied by cobalt and iron species together or 25% replacement of iron alone) surges the oxygen permeability by about 40%. This happens due to (i) a stable perovskite-type cubic structure with random distribution of anion vacancies at elevated temperatures, (ii) enlarged unit cell because of bigger Zr^{4+} ion insertion and thermal expansion, (iii) impending increase in O^{2-} vacancies following desorption of oxygen as molecules with simultaneous release of electrons, and (iv) enhanced surface reactions, i.e., improved dissociation of oxygen molecules at the front surface. At higher zirconium content ($y \geq 0.05$), the lower oxygen permeation capacity results because of (i) stabilization of the brownmillerite orthorhombic structure and (ii) emergence of $SrZrO_3$ as a secondary phase. These findings suggest that the dissolution limit of zirconium in $SrCo_{0.8}Fe_{0.2-y}Zr_yO_{3-\delta}$ lies below $y = 0.05$. It may be recalled that the above observation is consistent with that displayed by $La_{0.2}Ba_{0.8}Co_{0.8}Fe_{0.2-y}Zr_yO_{3-\delta}$ membrane (thickness 1 mm), i.e., enhancement of oxygen permeability upon raising y from 0 to 0.05; the values at 1000 °C being 1.1 and 2.69 ml/cm^2·min, respectively. Fan et al. [19] attributed increased oxygen permeation at 700–1000 °C in the perovskite cubic structure to random distribution of anion vacancies.

The oxygen permeability for all membranes is deduced for completeness and to demonstrate its inverse thickness dependence. J_{O2} in membrane (thickness > 0.3 mm) is governed by diffusion-controlled process and expressed at a temperature (T) as [9, 29].

$$J_{O2} = \{(RT)/(4F^2L)\}\ \sigma_O\ [(P_{OI})^{-n} - (P_{OE})^{-n}].$$

where R is the gas constant, $\sigma_O\ (P_O)^{-n}$ is the conductivity (σ; also proportional to anion vacancy concentration), F is flow rate of carrier gas, L is the membrane thickness, and P_O stands for the oxygen pressure

Table 4 Oxygen permeation flux (J_{O2}) data of $SrCo_{0.8}Fe_{0.2-y}Zr_yO_{3-\delta}$ ($y \leq 0.10$) membranes at different temperatures (air flow rate = 400 ml/min, helium flow rate = 45 ml/min)

Temp (°C)	J_{O2} (ml/cm^2 min)											
	(t = 1.0 mm) y equal to		(t = 1.5 mm) y equal to					(t = 2.0 mm) y equal to				
	0	0.050	0	0.025	0.050	0.075	0.100	0	0.025	0.050	0.075	0.100
700	0.46	0.66	0.4	0.44	0.52	0.37	0.33	0.34	0.38	0.45	0.31	0.28
800	1.01	1.49	0.83	0.93	1.2	0.7	0.63	0.68	0.76	0.94	0.59	0.51
900	1.65	2.34	1.41	1.56	1.99	1.24	1.11	1.13	1.26	1.53	1.01	0.87
1000	2.44	3.42	2.09	2.31	2.91	1.83	1.66	1.83	2.02	2.44	1.6	1.4

1 ml cm^{-2} min^{-1} = 7.44×10^{-7} mol cm^{-2} s^{-1}

(subscripts I and E representing inlet and exit side) with n as an exponent. Notice decrease in J_{O2} with increase in thickness (Figs. 8 and 10). Also, the objective has been to infer the optimum thickness displaying realistic J_{O2} with high mechanical stability. The results suggest that 1-mm-thick membrane conform to both these features/characteristics.

$SrCo_{0.8}Fe_{0.2-y}Zr_yO_{3-\delta}$ ($y = 0.05$) membrane corresponds to highest J_{O2} because of the zirconium (oxidation state 4 + and ionic radius 0.72 Å, larger than Fe^{4+} and Fe^{3+}) amount being just appropriate for inducing stability to the perovskite-type cubic phase besides creating random distribution of anion vacancies at elevated temperatures (≥ 800 °C) [22, 23, 27]. At other concentrations, the system shows (Fig. 5b) either the brownmillerite orthorhombic phase (Sr-deficient) with $SrZrO_3$ precipitation above 700–750 °C (for $y = 0.075$, 0.010) or a lone orthorhombic phase above 500 °C (for $y =$ 0.025). In both the cases, J_{O2} values are lower than displayed by cubic phase of compositions $y = 0$, 0.05 at ≥ 800 °C (Fig. 10). But, $SrCo_{0.8}Fe_{0.2}O_{3-\delta}$ (i.e., with no zirconium content $y = 0$) depicts lower J_{O2} and poor long-term stability vis-à-vis the compound having $y = 0.05$ (Figs. 10 and 12).

Ln (J_{O2}) vs. 1000/T plots for $SrCo_{0.80}Fe_{0.20-y}Zr_yO_{3-\delta}$ ($y =$ 0–0.10) membranes of thickness 1.0, 1.5, and 2.0 mm display linearity in the temperature range of 800–1000 °C. The activation energy obtained from the slope reveal decrease first but increase beyond zirconium concentration of $y = 0.05$. For example, E_A values of 1.5-mm-thick membrane found are 52.4, 50.3, 54.6, and 55 kJ/mol for $y = 0$, 0.05, 0.075, and 0.100, respectively. The decrease (or increase) in the activation energy is compatible with the increase (or decrease) observed in J_{O2}. This feature may be related to limited solubility of zirconium in $SrCo_{0.80}Fe_{0.20}O_{3-\delta}$ and precipitation of $SrZrO_3$ above a critical value of $y \sim 0.05$.

Membrane stability and reliability

To ascertain the structural stability of $SrCo_{0.8}Fe_{0.2}O_{3-\delta}$ membrane, XRD patterns of both the front and exit surfaces were recorded and analyzed after completion of three cycles of oxygen permeation measurements at 700, 800, 900, and 1000 °C in succession. XRD patterns of 1-mm-thick membrane depicted in Fig. 11 reveal clearly the existence of only perovskite-type cubic phase on both sides after three oxygen permeation cycles at 700–1000 °C covering a total time of about 24 h. Obviously, the $SrCo_{0.8}Fe_{0.2}O_{3-\delta}$ disc remains stable all through the operation cycles. Nevertheless, for practical applications, the membrane should be reliable in terms of oxygen permeability as well as long-term stability. To investigate this aspect, (J_{O2}) of $SrCo_{0.8}Fe_{0.2}O_{3-\delta}$ membrane (thickness 1.5 mm) was monitored at 900 °C for 120 h through a continuous operation by setting the flow rates of input air at front surface and carrier helium gas at exit side as 400 ml/min and 45 ml/min, respectively (Fig. 12a). Notice that the J_{O2} figure was sustained at ~ 1.41 ml/cm^2·min for barely 60 h and fell thereafter by ~ 7% during the next 60 h. Undoubtedly, this J_{O2} value is above 1.0 ml/cm^2·min set for economic and industrial viability considerations [53], yet the long-term stability of the membrane remained poor and caused concern. In this context, partial substitution of iron with zirconium in $SrCo_{0.8}Fe_{0.2}O_{3-\delta}$ was rather advantageous. For example, the oxygen permeation flux of $SrCo_{0.80}Fe_{0.15}Zr_{0.05}O_{3-\delta}$ membrane (thickness 1.5 mm) measured at 900 °C shows a constant higher value of 1.99 ml/cm^2·min for 120 h (Fig. 12b). Obviously, zirconium incorporation has not only caused significant improvement in (J_{O2}) but also induced marked stability in the $SrCo_{0.80}Fe_{0.20}O_{3-\delta}$ membrane. Also, its XRD patterns before and after carrying out the oxygen permeation exercise at 900 °C for 120 h (shown in Fig. 13) indicate continual presence of perovskite-type cubic phase and so the structural stability of the membrane. Similarly, $SrCo_{0.8}Fe_{0.2}O_{3-\delta}$ membrane (thickness 1 mm) exhibits high oxygen permeation flux J_{O2} of ~ 2.44 ml/cm^2·min (or 1.8×10^{-6} mol cm^{-2} s^{-1}) at 1000 °C but shows inadequate long-term stability. However, zirconium substitution of iron (i) makes the perovskite-type cubic phase stable in the temperature range 800–1000 °C with lattice parameter $a = 3.9629$–3.9873 Å; (ii) enhances J_{O2} by ~ 40%, i.e., to ~ 3.42 ml/cm^2·

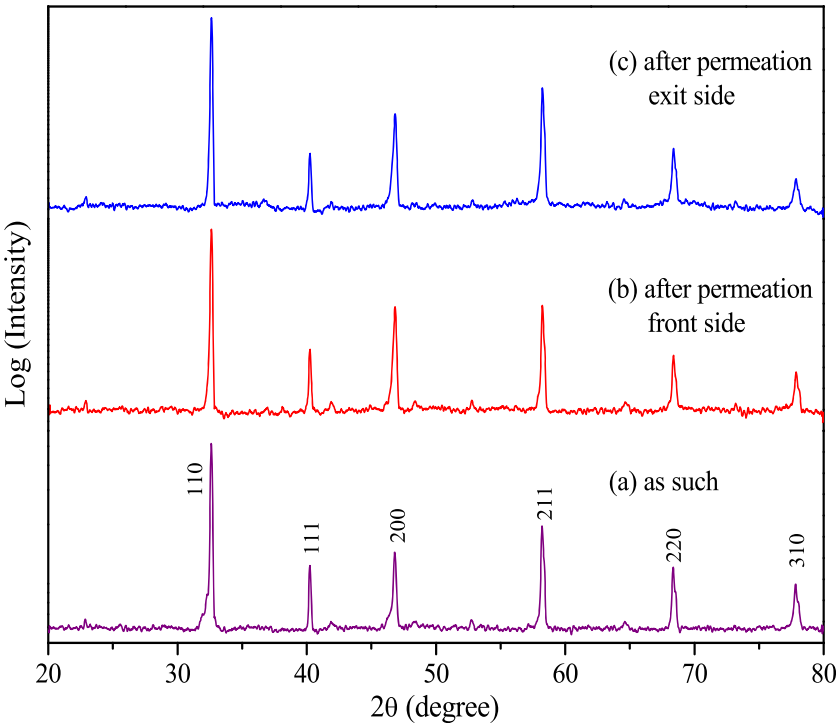

Fig. 11 X-ray diffraction patterns of $SrCo_{0.8}Fe_{0.2}O_{3-\delta}$ membrane (a) as such or before and (b, c) after oxygen permeation process; (b) front/entrance, and (c) back/exit side

min at 1000 °C in $SrCo_{0.8}Fe_{0.2-y}Zr_yO_{3-\delta}$ ($y = 0.05$) membrane of thickness 1 mm (Fig. 10a); and (iii) sustains steady oxygen permeation for a longer duration (for at least 120 h at 900 °C). The increase in oxygen permeation flux can be attributed to (a) enlarged perovskite-type cubic unit cell and (b) additional anion vacancies produced by weakening of metal-oxygen bond (brought via thermal expansion) and gaining energy at elevated temperatures. The significant rise observed in oxygen permeability itself is indicative of extra anion vacancies.

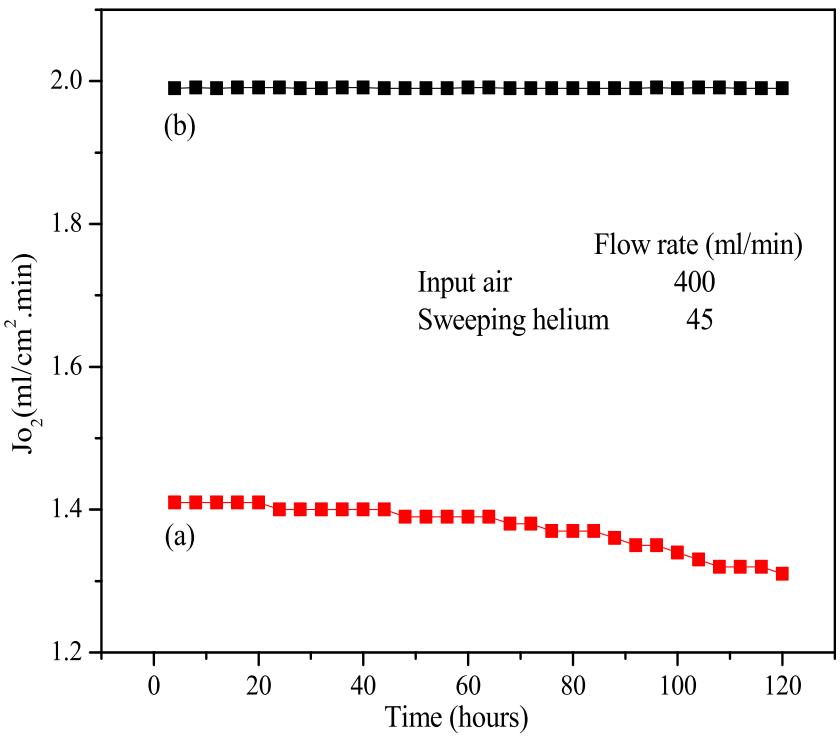

Fig. 12 The variation of oxygen permeation flux (J_{O2}) for (a) $SrCo_{0.80}Fe_{0.20}O_{3-\delta}$, (b) $SrCo_{0.80}Fe_{0.20-y}Zr_yO_{3-\delta}$ ($y = 0.05$) membranes (thickness = 1.5 mm) held at 900 °C for 120 h. (unit being 1 ml cm^{-2} min^{-1} = 7.44×10^{-7} mol cm^{-2} s^{-1})

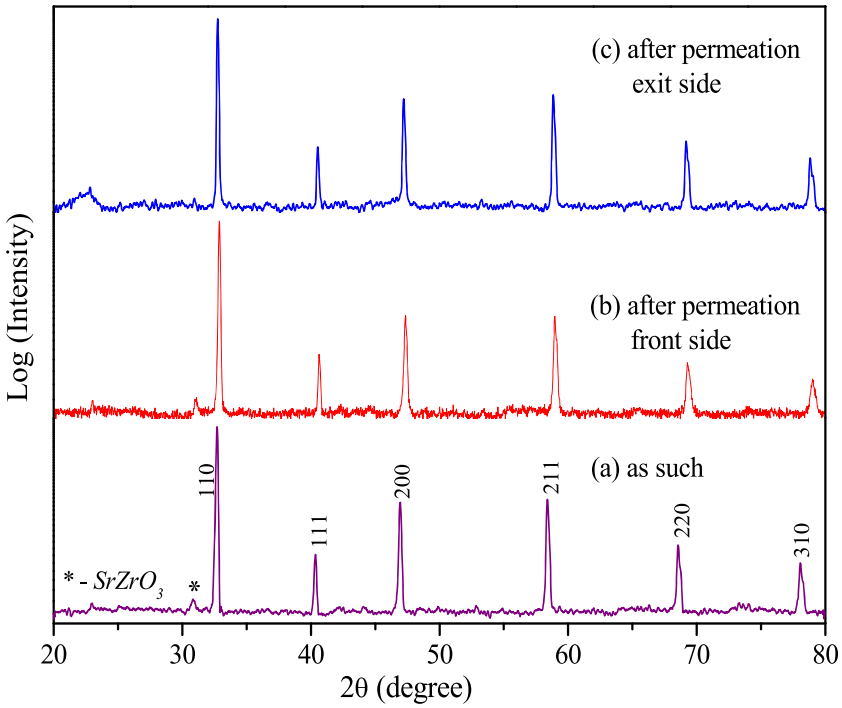

Fig. 13 X-ray diffraction patterns of $SrCo_{0.80}Fe_{0.20-y}Zr_yO_{3-\delta}$ (y = 0.05) membrane (a) as such, (b, c) after oxygen permeation at 900 °C for 120 h, (b) front/entrance, and (c) back/exit side. The $SrZrO_3$ peak is marked with asterisk (*)

Conclusions

A single perovskite-type cubic phase of $SrCo_{0.8}Fe_{0.2}O_{3-\delta}$ (a = 3.8650 ± 0.0002 Å, Z = 1), produced by decomposition of sol-gel derived oxalate precursor at 1150 °C for 5 h, remains stable in the temperature range 800–1000 °C. It is characterized by a high oxygen permeability flux of J_{O2} ~ 1.65 ml/cm^2·min (or 1.23 × 10^{-6} mol cm^{-2} s^{-1}) at 900 °C for 1-mm-thick membrane; J_{O2} is maintained continuously for ~ 60 h only at 900 °C. The 5% zirconium incorporation at Co/Fe site (i) enlarges the perovskite-type cubic unit cell exhibiting a = 3.9629–3.9873 Å in the temperature range of 800–1000 °C, (ii) raises J_{O2} to ~ 2.34 ml/cm^2·min (or 1.74 × 10^{-6} mol cm^{-2} s^{-1}) at 900 °C, and (iii) improves phase stability and sustains oxygen permeation for much longer duration (i.e., 120 h at least). The formation of a perovskite-type cubic phase in Sr–Co–Fe–O system with abundance of anion vacancies is crucial for both the high oxygen permeation and extended operational stability at elevated temperatures (800–1000 °C). This can be achieved by partial substitution of iron with zirconium, optimum composition being $SrCo_{0.8}Fe_{0.2-y}Zr_yO_{3-\delta}$ (y = 0.05).

References

1. Hashim SM, Mohamed AR, Bhatia S (2010) Current status of ceramic-based membranes for oxygen separation from air. Adv Colloid Interf Sci 160:88–100
2. Teraoka Y, Honbe Y, Ishii J, Furukawa H, Moriguchi I (2002) Catalytic effects in oxygen permeation through mixed-conductive LSCF perovskite membranes. Solid State Ionics 152–153:681–687
3. Bouwmeester HJM, Burggraaf AJ (1996) Fundamentals of inorganic membrane science and technology. Elsevier, Amsterdam Chapter 10
4. Hong WK, Choi GM (2010) Oxygen permeation of BSCF membrane with varying thickness and surface coating. J Membr Sci 346: 353–360
5. Shao Z, Xiong G, Cong Y, Yang W (2000) Synthesis and oxygen permeation study of novel perovskite-type $BaBi_xCo_{0.2}Fe_{0.8-x}O_{3-\delta}$ ceramic membranes. J Membr Sci 164:167–176
6. Vashook VV, Daroukh MA, Ullmann H (2001) Oxygen ion diffusion in perovskite-type oxides determined by permeation and by relaxation measurements. Ionics. 7:59–66
7. Zeng P, Shao Z, Liu S, Xu ZP (2009) Influence of M cations on structural, thermal and electrical properties of new oxygen selective membranes based on $SrCo_{0.95}M_{0.05}O_{3-\delta}$ perovskite. Sep Purif Technol 67:304–311
8. Li K (2007) Ceramic membrane for separation and reaction. John Wiley, England Chapter 6
9. Sunarso J, Baumann S, Serra JM et al (2008) Mixed ionic–electronic conducting (MIEC) ceramic-based membranes for oxygen separation. J Membr Sci 320:13–41
10. Teraoka Y, Nobunaga T, Yamazoe N (1988) Effect of cation substitution on the oxygen semipermeability of perovskite-type oxides. Chem Lett 3:503–506
11. Teraoka Y, Zhang HM, Furukawa S, Yamazoe N (1985) Oxygen permeation through perovskite-type oxides. Chem Lett:1743–1746
12. Xinfa D, Heng Z, Weiming L (2008) Preparation and characterization of a perovskite-type mixed conducting $SrFe_{0.6}Cu_{0.3}Ti_{0.1}O_{3-\delta}$ membrane for partial oxidation of methane to syngas. Chin J Chem Eng 16(3):411–415
13. Li Y, Zhao H, Xu N et al (2010) Systematic investigation on structure stability and oxygen permeability of Sr-doped $BaCo_{0.7}Fe_{0.2}Nb_{0.1}O_{3-\delta}$ ceramic membranes. J Membr Sci 362:460–470
14. Wang W, Cong Y, Yang W (2002) Oxygen permeation study in a tubular $Ba_{0.5}Sr_{0.5}Co_{0.8}Fe_{0.2}O_{3-\delta}$ oxygen permeable membrane. J Membr Sci 210:259–271
15. Bouwmeester HJM, Kruidhof H, Burggraaf AJ (1994) Importance of the surface exchange kinetics as rate limiting step in oxygen

permeation through mixed-conducting oxides. Solid State Ionics 72:185–194
16. McIntosh S, Vente JF, Haije WG, Blank DHA, Bouwmeester HJM (2006) Phase stability and oxygen non-stoichiometry of $SrCo_{0.8}Fe_{0.2}O_{3-\delta}$ measured by in situ neutron diffraction. Solid State Ionics 177:833–842
17. Kruidhof H, Bouwmeester HJM, Doorn RHE, Burggraaf AJ (1993) Influence of order-disorder transitions on oxygen permeability through selected nonstoichiometric perovskite-type oxides. Solid State Ionics 63–65:816–822
18. Qiu L, Lee TH, Liu LM, Yang YL, Jacobson AJ (1995) Oxygen permeation studies of $SrCo_{0.8}Fe_{0.2}O_{3-\delta}$. Solid State Ionics 76:321–329
19. Fan CG, Deng ZQ, Zuo YB, Liu W, Chen CS (2004) Preparation and characterization of $SrCo_{0.8}Fe_{0.2}O_{3-\delta}$–$SrSnO_3$ oxygen-permeable composite membrane. Solid State Ionics 166:339–342
20. Lu H, Cong Y, Yang W (2007) Oxygen permeability and improved stability of a permeable Zr-substituted perovskite membrane for air separation. Mater Sci Eng B 141:55–60
21. Liu H, Zhu Z, Cong Y, Zhang T, Yang W (2012) Remarkable dependence of electrochemical performance of $SrCo_{0.8}Fe_{0.2}O_{3-\delta}$ on A-site on stoichiometry. Phys Chem Chem Phys 14:7234–7239
22. Yang L, Tan L, Gu X, Jin W, Zhang L, Xu N (2003) A new series of $Sr(Co,Fe,Zr)O_{3-\delta}$perovskite-type membrane materials for oxygen permeation. Ind Eng Chem Res 42:2299–2305
23. Yang L, Gu X, Tan L, Zhang L, Wang C, Xu N (2003) Role of ZrO_2 addition on oxygen transport and stability of ZrO_2-promoted $SrCo_{0.4}Fe_{0.6}O_{3-\delta}$. Sep Purif Technol 32:301–306
24. Fan CG, Zuob YB, Li JT, Lu JQ, Chen CS, Bae DS (2007) Highly permeable $La_{0.2}Ba_{0.8}Co_{0.8}Fe_{0.2-x}Zr_xO_{3-\delta}$membranes for oxygen separation. Sep Purif Technol 55:35–39
25. Yao W, Cheng H, Zhao H et al (2016) Synthesis, oxygen permeability, and structural stability of $BaCo_{0.7}Fe_{0.3-x}Zr_xO_{3-\delta}$ ceramic membranes. J Membr Sci 504:251–262
26. Li S, Jin W, Huang P et al (1999) Perovskite-related ZrO_2 -doped $SrCo_{0.4}Fe_{0.6}O_{3-\delta}$membrane for oxygen permeation. AICHE J 45(2):276–284
27. Chen W, Zuo YB, Chen CS, Winnubst AJA (2010) Effect of Zr^{4+} doping on the oxygen stoichiometry and phase stability of $SrCo_{0.8}Fe_{0.2}O_{3-\delta}$ oxygen separation membrane. Solid State Ionics 181:971–975
28. Lu H, Deng ZQ, Tong J, Yang W (2005) Oxygen permeability and structural stability of Zr-doped oxygen-permeable $Ba_{0.5}Sr_{0.5}Co_{0.8}Fe_{0.2}O_{3-\delta}$ membrane. Mater Lett 59:2285–2288
29. Qi X, Lin YS, Swartz SL (2000) Electric transport and oxygen permeation properties of lanthanum cobaltite membranes synthesized by different methods. Ind Eng Chem Res 39:646–653
30. Martynczuk J, Arnold M, Feldhoff A (2008) Influence of grain size on the oxygen permeation performance of perovskite-type $(Ba_{0.5}Sr_{0.5})(Fe_{0.8}Zn_{0.2})O_{3-\delta}$membranes. J Membr Sci 322:375–382
31. Jaiswal SK, Kashyap VK, Kumar J (2012) On the sol–gel synthesis and characterization of strontium ferrite ceramic material. Mater Res Bull 47:692–699
32. Kashyap VK, Jaiswal SK, Kumar J (2016) On the structural stability and oxygen permeation behaviorof inorganic $SrCo_{0.8}Fe_{0.2}O_{3-\delta}$ membranes. Ionics. 22:2471–2485
33. Kumar A, Kumar J (2008) On the synthesis and optical absorption studies of nano-size magnesium oxide powder. J Phys Chem Solids 69:2764–2772
34. Nagai T, Ito W, Sakon T (2007) Relationship between cation substitution and stability of perovskite structure in $SrCoO_{3-\delta}$-based mixed conductors. Solid State Ionics 177:3433–3444
35. Wu Z, Dong X, Jin W, Fan Y, Xu N (2007) A dense oxygen separation membrane deriving from nanosized mixed conducting oxide. J Membr Sci 291:172–179
36. Deng ZQ, Yang WS, Liu W, Chen CS (2006) Relationship between transport properties and phase transformations in mixed-conducting oxides. J Solid State Chem 179:362–369
37. He Y, Zhu X, Guo Z, Yang W (2010) Phase transitions in $Sr_{1+x}Co_{0.8}Fe_{0.2}O_{3-\delta}$ oxides. Mater Lett 64:1618–1621
38. Shin MJ, Yu JH (2012) Oxygen transport of A-site deficient $Sr_{1-x}Fe_{0.5}Co_{0.5}O_{3-\delta}$(x = 0–0.3) membranes. J Membr Sci 401–402: 40–47
39. McIntosh S, Vente JF, Haije WG, Blank DHA, Bouwmeester HJM (2006) Structure and oxygen stoichiometry of $SrCo_{0.8}Fe_{0.2}O_{3-\delta}$ and$Ba_{0.5}Sr_{0.5}Co_{0.8}Fe_{0.2}O_{3-\delta}$. Solid State Ionics 177:1737–1742
40. Jaiswal SK, Kumar J (2011) On the sol–gel synthesis and structure, optical, magnetic and impedance behaviour of strontium cobaltite powder. J Alloys Compd 509:3859–3865
41. Didier C, Claridge J, Rosseinsky M (2014) Crystal structure of brownmillerite Ba_2InGaO_5. J Solid State Chem 218:38–43
42. Goodenough JB, Ruiz-Diaz JE, Zhen YS (1990) Oxide-ion conduction in $Ba_2In_2O_5$ and $Ba_3In_2MO_8$ (M=Ce, Hf, or Zr). Solid State Ionics 44:21–31
43. Young V, Otagawa T (1985) XPS studies on strontium compounds. Appl Surf Sci 20:228–248
44. Zhang HL, Wang DZ, Yang B, Huang NK (1997) XPS measurement for the elements in the interface between oxygen ion irradiated$ZrO_2 - Y_2O_3$ films and iron substrate. Phys Status Solidi 160:145–150
45. Jiratova K, Mikulova J, Klempa J, Grygar T, Bastl Z, Kovanda F (2009) Modification of Co–Mn–Al mixed oxide with potassium and its effect on deep oxidation of VOC. Appl Catal A 361:106–116
46. Bu Y, Zhong Q, Xu D, Tan W (2013) Redox stability and sulfur resistance of $Sm_{0.9}Sr_{0.1}Cr_xFe_{1-x}O_{3-\delta}$ perovskite materials. J Alloys Compd 578:60–66
47. Dupin JC, Gonbeau D, Benqlilou-Moudden H, Vinatier P, Levasseur A (2001) XPS analysis of new lithium cobalt oxide thin-films before and after lithium deintercalation. Thin Solid Films 384:23–32
48. Norman C, Leach C (2011) In situ high temperature X-ray photoelectron spectroscopy study of barium strontium iron cobalt oxide. J Membr Sci 382:158–165
49. Grosvenor AP, Kobe BA, Biesinger MC, McIntyre NS (2004) Investigation of multiplet splitting of Fe 2p XPS spectra and bonding in iron compounds. Surf Interface Anal 36:1564–1574
50. Machocki A, Ioannides T, Stasinska B et al (2004) Manganese–lanthanum oxides modified with silverfor the catalytic combustionof methane. J Catal 227:282–296
51. Alaee MA, Movahednia MM, Mohammadi T (2009) Effect of Ba content on oxygen permeation performance of $Ba_xSr_{1-x}Co_{0.8}Fe_{0.2}O_{3-\delta}$($x$ =0.2, 0.5, and 0.8) perovskite-type membrane. J Chem Eng Data 54:3082–3091
52. Hench LL, West JK (1990) The sol-gel process. Chem Rev 90:33–72
53. Steele BCH (1992) Oxygen ion conductors and their technological applications. Mater Sci Eng B13:79–87